2015-01-01

A Tectonic Analysis On The Central Region Of The Himalaya Collision Zone Using Double Difference Tomography

Chanel Perez
University of Texas at El Paso, cperez005@verizon.net

A TECTONIC ANALYSIS ON THE CENTRAL REGION OF THE HIMALAYA COLLISION ZONE USING DOUBLE DIFFERENCE TOMOGRAPHY

CHANEL ASHLIE PEREZ

Department of Geological Sciences

APPROVED:

Aaron Velasco, Ph.D., Chair

Diane Doser, Ph.D.

Martine Ceberio, Ph.D.

Charles Ambler, Ph.D.
Dean of the Graduate School

A TECTONIC ANALYSIS ON THE CENTRAL REGION OF THE HIMALAYA COLLISION ZONE USING DOUBLE DIFFERENCE TOMOGRAPHY

by

Chanel A. Perez, B.S.

THESIS

Presented to the Faculty of the Graduate School of

THE UNIVERSITY OF TEXAS AT EL PASO

in Partial Fulfillment

of the Requirements

for the Degree of

MASTER OF SCIENCE

Department of Geological Sciences

THE UNIVERSITY OF TEXAS AT EL PASO

May 2015

Acknowledgements

I would like to thank Dr. Lennox Thompson, Ezer Patlan, and Richard Alfaro-Diaz for their help throughout my research of central Himalaya. These peers have provided me knowledge on scripting, coding and mapping that I use throughout this project. I met all three students in fall 2013 and was happy to learn that we have all gone through similar challenges in completing our geophysics degrees. Without them, my geophysical skills wouldn't be what they are today.

Also, a thanks to my mentor at Los Alamos National Laboratory, Dr. Monica Maceira and her post doc Ellen Syracuse. Monica and Ellen both introduced me to tomographic techniques and inversion methods used in Geophysics. Unfortunately, I didn't have the opportunity to take the inverse theory course offered during my time at The University of Texas at El Paso. Both of these dedicated scientists provided me a great replacement for that knowledge.

Lastly, a special thanks to my thesis advisor Dr. Aaron Velasco. I first met Aaron when I enrolled in his Seismology class in fall 2013. His research and previous work experience inspired me so much that he instilled in me a personal goal to follow a path much similar to his. Aaron prides himself in his mentoring philosophy, but there are two aspects of his philosophy that I really enjoyed, one of them being his open-door policy. Without this policy I would have never felt comfortable enough to ask him questions on concepts I was unsure of. The other aspect was his drive to challenge his students. It did not matter where I was in my project or where I had to be, Aaron always openly accepted my work, rolled with how much I had left to do and gave me my next challenge. Without that pressure, I was able to work efficiently and effectively. My advisor has provided me so much opportunity as a young scientist that I now have my first job as a career geophysicist. Without his efforts to keep me motivated and on course, I wouldn't have become the scientist I am today.

Abstract

The Himalaya mountain range remains the only place on Earth undergoing continuous effects from the continental-continental collision between India and Asia. Because of this, the Himalayas have been subjected to extensive deformation and transpression, and contain five major shear zones. Extensive seismic analysis of the region, however, is lacking due to sparse seismograph coverage and complexity of the crustal structure. I examined seismic event data from two temporary seismic networks deployed in the central Himalaya, the HIMNT deployment from 2001-2003, and the Bhutan deployment from 2002-2003. Using this data I develop a 3-D earth model for the region using double-difference tomography, TomoFDD. I specifically focused on 223 regional events surrounding the thirty-four stations that comprise both networks. All events are located between 82° and 98°E longitude, and 22° and 34°N latitude, and with depths between 10 and 700 km. Prior analysis of both datasets consisted of event location, relocation, and 1D velocity modeling. Using TomoFDD I performed event relocations and developed a 3-D model that resolves the velocity structure of some areas of the central Himalaya between 25km and 150km. I also find that the velocity model for 45 km and 60 km may be consistent with the proposed model of channel flow beneath the Himalayas.

Table of Contents

Tables

List of Figures

Chapter 1: Introduction

The Himalaya region lacks both seismic data and analysis due lack of station coverage and crustal complexity. This region remains the only place on Earth undergoing continuous effects from the continental-continental collision between India and Asia during the Paleogene (Dewey and Bird, 1970; Dewey and Burke, 1973; Molnar and Tapponnier, 1975; Hodges, 2000). Without earthquake data or analysis, the region cannot be analyzed for seismic hazards or crustal evolution. Retrieving data will give insight into continental accretion characteristics, earthquake-deformation relationships, and the crustal evolution of the Himalayas.

In January 2002, a temporary seismic network was deployed in the Kingdom of Bhutan (Velasco et al., 2007). The goal of this deployment was to understand seismic hazard of the region and influence the installation of a permanent seismic network. This network recorded continuous earthquake data until March of 2003 and recorded over 2,000 local, regional and teleseismic events. The installation consisted of five broadband stations, four of which were distributed along the Western edge of Bhutan (Figure 1). Preliminary analysis of the deployment showed areas of intense deformation relating to shear stress (Velasco et al., 2007). These results were found by verifying event locations, examining earthquake phases, and performing 1-D velocity modeling (Gee, 2005).

During this same time frame, another temporary network was active in Nepal and Tibet starting in September 2001. This deployment was called The Himalaya Nepal Tibet Experiment, HIMNT (Figure 1; de la Torre et al., 2005). The goal of this deployment was to determine if deep earthquakes specific to eastern Nepal and southern Tibet occurred at lower crust or upper mantle depths. This network recorded continuous data until April of 2003 and recorded over 1,500 local earthquake events. The installation consisted of 27 broadband stations distributed throughout central Asia (de la Torre et al., 2006).

I leveraged the initial 1D velocity model (Figure 2; Gee, 2005) developed from the temporary network deployed in Bhutan to develop a 3D velocity model for the central portion of

the Himalaya using the double-difference tomographic inversion technique, tomoFDD (Zhang and Thurber, 2003) for regional data. I began initial 3D modeling using the five-station deployment in Bhutan and ~150 regional earthquake events. I found that that the regional data recorded on this networks did not allow for resolution adequate for tectonic interpretation. With initial models displaying poor resolution, I utilized stations from the Himalaya Nepal Tibet Experiment and incorporated additional regional events to increase resolution and develop a 3D model over a larger swath.

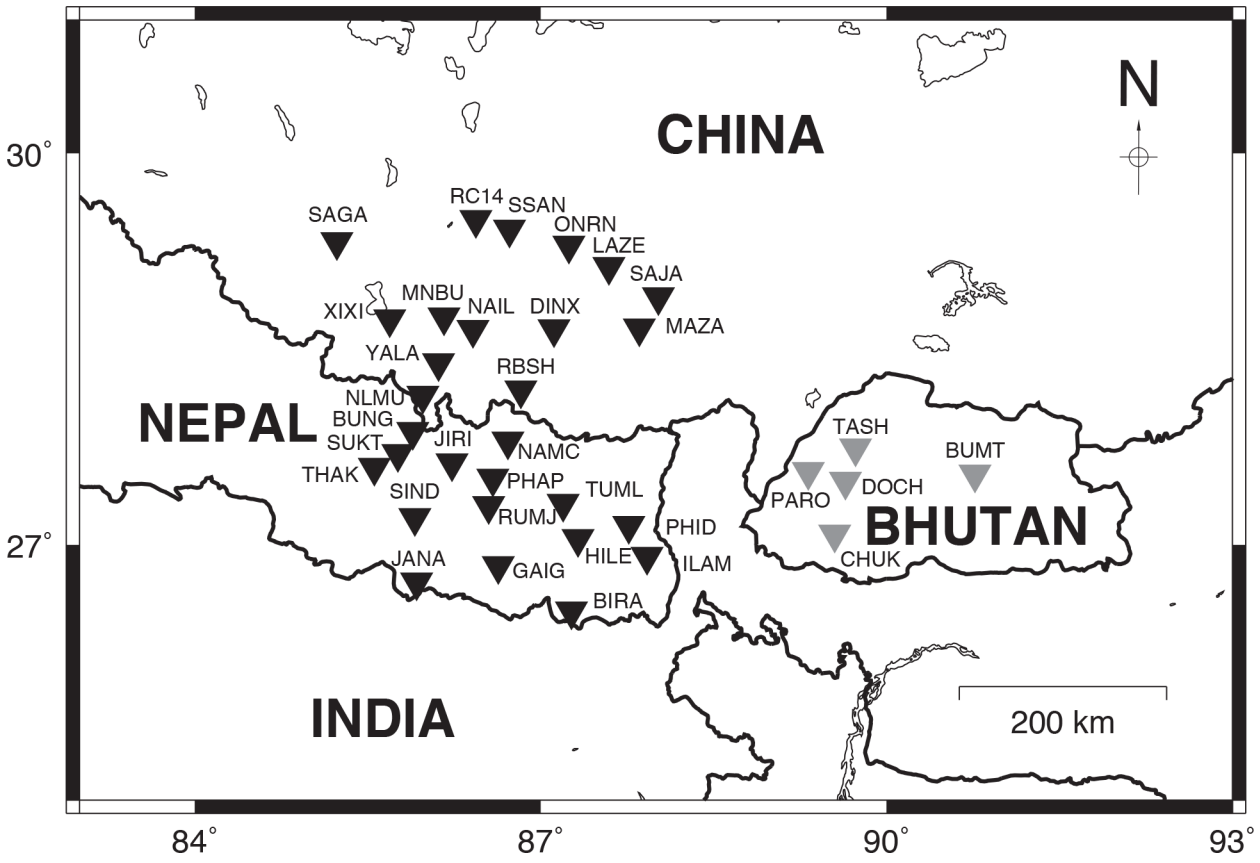

Figure 1: Map of Bhutan (inverted black triangles) and HIMNT temporary seismic networks (inverted grey triangles).

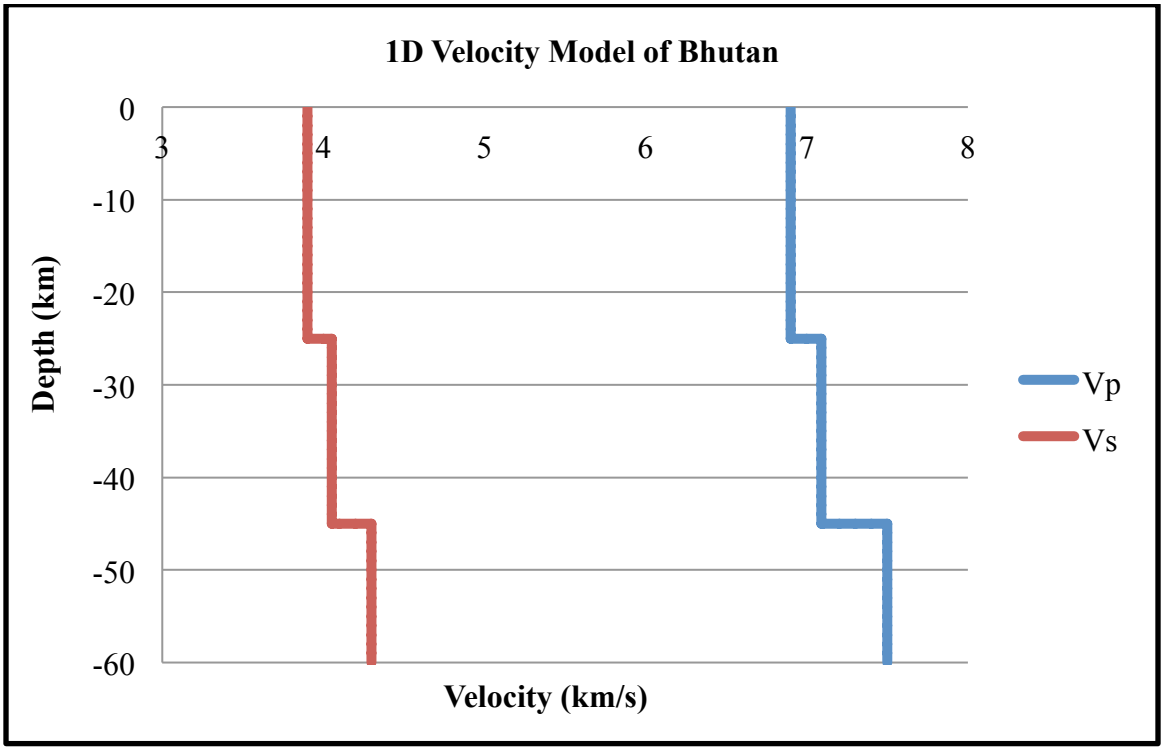

Figure 2: 1D velocity model developed by Gee (2005) at the termination of the Bhutan temporary network.

Chapter 2: Tectonic Setting

2.1 Deformational Zones

The Himalaya suture zone was formed by the massive continental-continental collision between India and Eurasia during the Paleogene (Dewey and Bird, 1970; Dewey and Burke, 1973; Molnar and Tapponnier, 1975; Hodges, 2000). The rate of relative motion from when the Indian plate began its ascent toward Eurasia during late Cretaceous until its collision in the Paleogene was between 100-180 mm/year (Molnar and Tapponnier, 1975). Toward the end of the Paleogene, the rate of convergence dropped down to ~150 to ~40 mm/yr. as the orogeny formed and the Tibetan Plateau began to uplift (Copley et al., 2010; Khanal et al., 2015). Molnar and Tapponnier (1975) suggest that a minimum of 1500 km of relative plate motion between Eurasia and India can be assumed to be deformation of continental lithosphere (Molnar and Tapponnier, 1975; Mattauer, 1986). The deformation is not just limited to the suture zone but rather spread out throughout the collision zone (Molnar and Tapponnier, 1975; Mattauer, 1986). This distribution implies extensive crustal thickening as a result of faulting and folding (Molnar and Tapponnier, 1975). Molnar and Tapponnier (1975) also state that previous geologic, seismic and gravity data suggest a northward under-thrusting of the Indian subcontinent which would support the deformation extending beyond the collision zone.

After the rate of convergence slowed, the deformation migrated southward in Tibet (Burg et al., 1987; Ratschbacher et al., 1994) and then further south through Nepal, again accompanied by thrusting and shearing in the Greater Himalaya, (Kohn et al., 2004; Goscombe et al., 2006; Carosi et al., 2007, 2010; Corrie and Kohn, 2011; Imayama et al., 2012; Montomoli et al., 2013) the area between the Main Central Thrust and the South Tibetan Detachment System (Figure 3). From the initiation of the collision to the migration of the deformation, five intricate shear zones of the Himalayas were created: Main Frontal Thrust (MFT), the Main Boundary Thrust (MBT), the Main Central Thrust (MCT), the South Tibetan Detachment System (STDS) and the Indus-

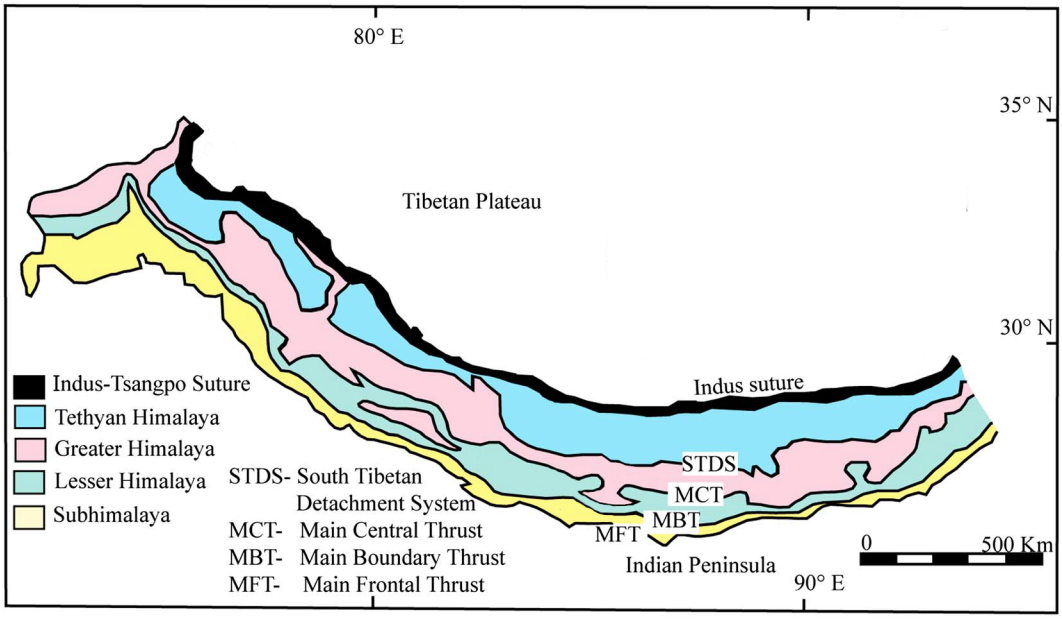

Figure 3: Map of the Himalayas 5 major shear zones in relation to the higher Himalaya, the Tibetan Plateau and the lesser Himalaya, the Indian shield (modified from Khanal et al., 2015).

Tsangpo Suture Zone (ITSZ) (Figure 3). The MCT is the separation between the lesser Himalaya region, the Indian shield, and the high Himalaya region, the Tibetan Plateau (Figure 3). Located directly above the MCT is the ITSZ. Initial convergence between India and Asia started along this suture zone. Convergence continued even after its closure (Ni and Barazangi, 1984) and the MBT became the new boundary for continental convergence (LeFort, 1975).

2.2 Fault Orientations

Both the MCT and MBT are regions of over-thrusting and folds with supporting mineralogy of medium-grade metamorphism (LeFort, 1975). While Seeber et al. (1981) suggest that the MBT and MCT are contemporaneous features instead of occurring successively; their findings support a compressional region with thrust faulting. They created a model showing the presence of a Basement Thrust (BT) where the Indian plate décollement meets the MCT (Figure 4).

Drupka et al. (2006) proves additional fault orientations exist within central Himalaya by identifying strike-slip focal mechanisms (Figure 5). Specifically, they perform event relocations and determine the nature of deformation of Bhutan for events occurring between 1937 and 2003. The proximity of relocated earthquakes to original locations after 1964 suggests Bhutan has been seismically active for the past 60 years with focal mechanisms showing strike-slip deformation (Drupka et al., 2006). This finding suggests that there is additional deformation beyond the predominant thrust faulting observed at the surface.

The Himalayan Nepal Tibet PASSCAL Seismic Experiment (HIMNT) also examined seismicity and geologic structure in Central Himalaya, specifically in southern Tibet, Tibet and eastern Nepal (Sheehan et al., 2008). This deployment was initiated in 2001 and ended in early 2003. Results of this experiment also focus on Central Himalaya structural make-up: strike-slip faulting beneath the Moho with normal faulting in the upper crust, which supports the idea that

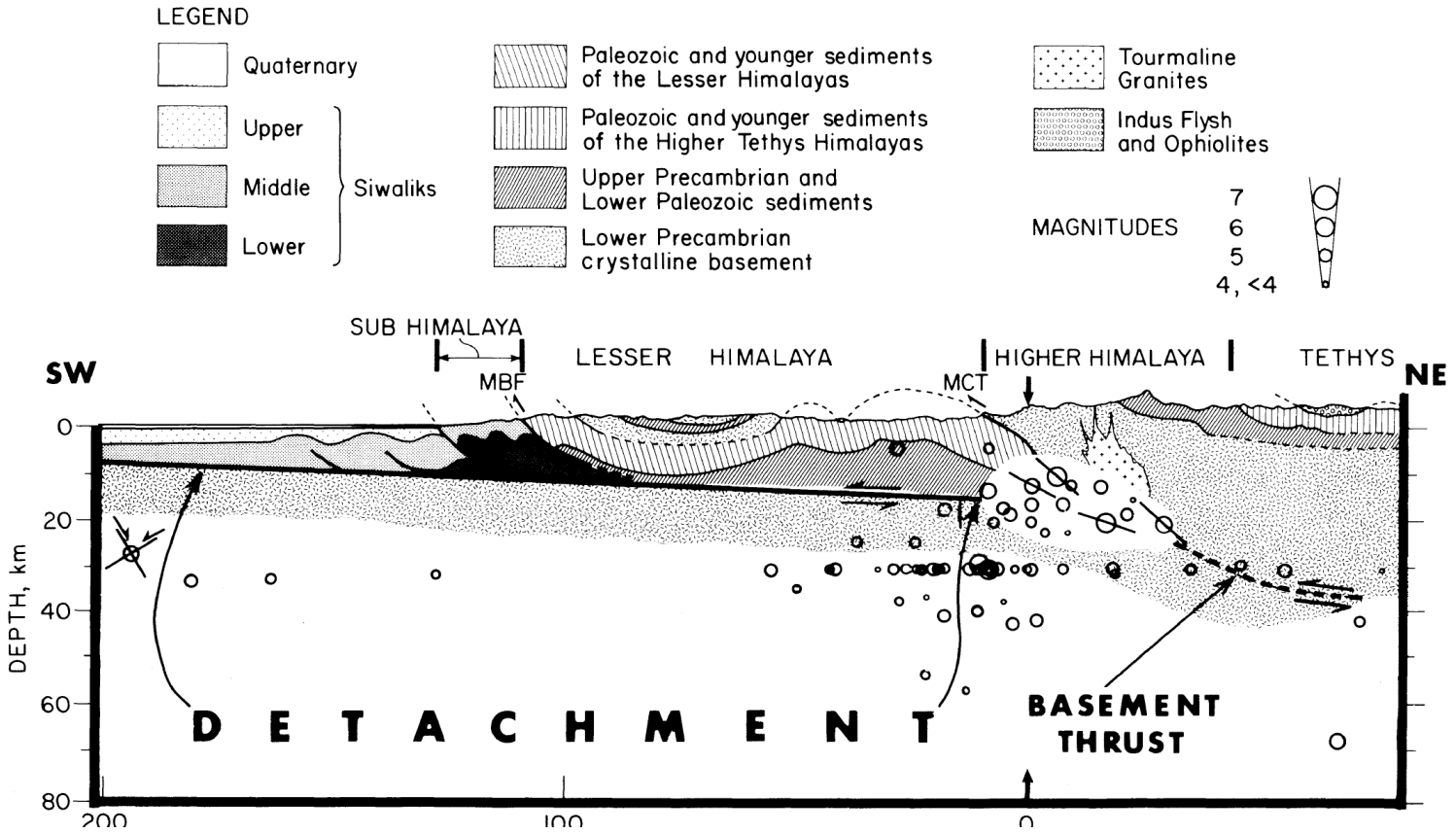

Figure 4: Cross-section displaying the transition zone between the lesser Himalaya Indian Plate detachment and the Basement Thrust of the higher Himalaya with associated earthquake magnitudes (modified from Seeber et al., 1981).

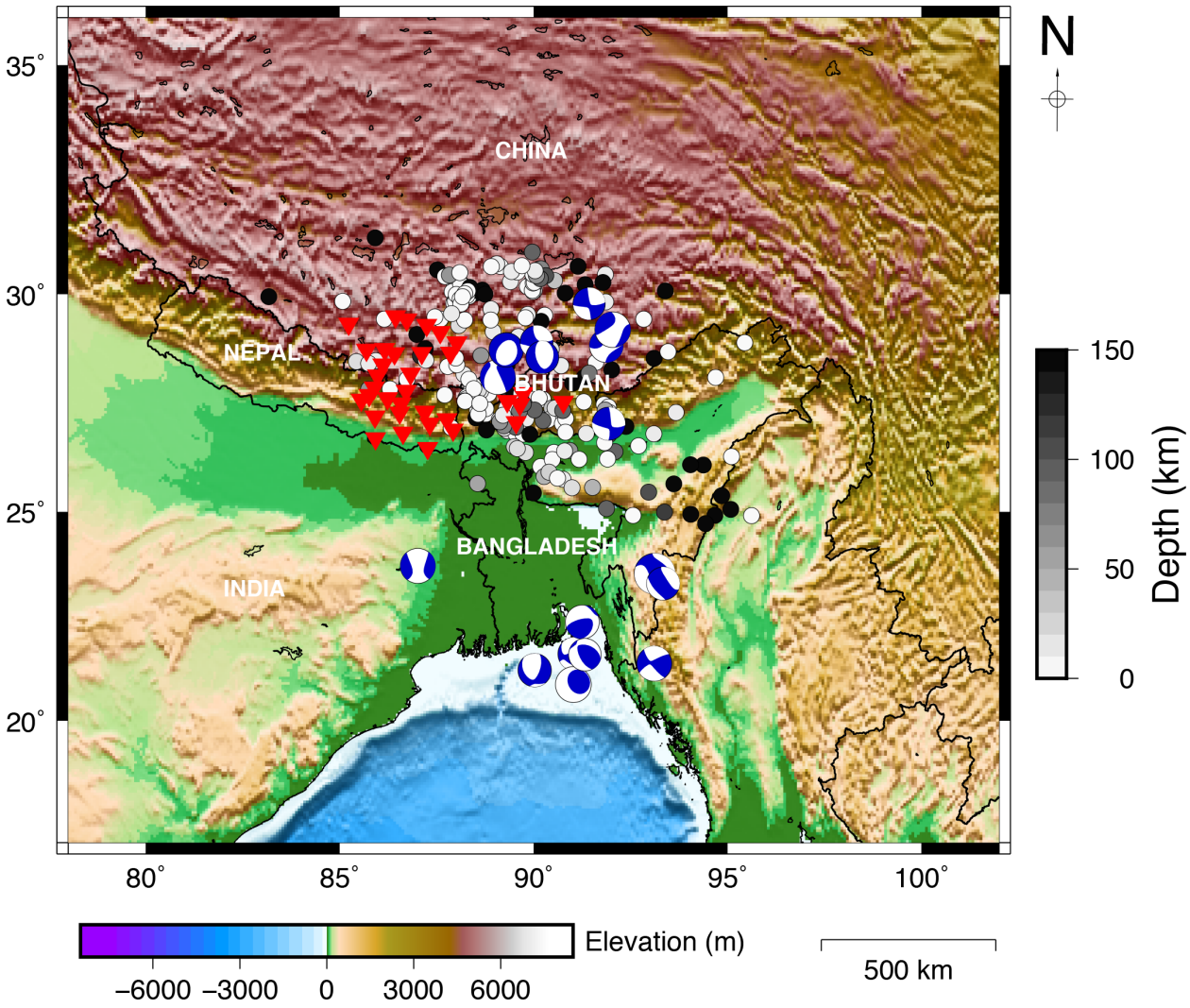

Figure 5: Map showing Bhutan seismic network (Velasco et al., 2007) and HIMNT seismic network (de la Torre et al., 2005) as red inverted triangles distributed throughout central Himalaya. 223 regional events (black and white circles) are shown along with Harvard Centroid Moment Tensor solutions from January 2001-December 2003.

additional deformation beyond the thrusting observed at the surface (Drupka et al., 2006) exists. Sheehan et al. (2008) suggest that these differing fault orientations reflect a transition from deformation driven by body forces in the crust to plate boundary forces in the upper mantle. Receiver function analysis of the HIMNT shows an anisotropic medium interpreted as the décollement between the Himalaya and Indian plate (Sheehan et al., 2008).

2.3 Seismic Activity

Geophysical evidence shows that south of the Himalaya, India's basement rock does not flex and slide beneath the Himalaya steadily, but it lurches during great earthquakes (Seeber and Armbruster, 1981; Molnar, 1990; Bilham, 2001). There have been multiple great earthquakes since the early 1800s that mark these significant rupture periods around the Central Himalaya region. These earthquakes have occurred in 1803, 1833, 1897, 1905, 1934, and 1950 (Bilham et al., 2001). The 1803 earthquake of M ~8 caused extensive damage in northern India while the 1833 Nepal earthquake and 1905 Kangra earthquake had rupture lengths ~120 km with estimated Ms of 7.7 to 7.8 (Bilham 1995, 2001; Ambraseys et al., 2000; Bilham et al., 2001). The 1897 8.1 Ms Shillong earthquake occured 100 km south of Himalaya and did not relieve strain along the main Himalayan thrusts (Bilham and England, 2001; Bilham et al., 2001). When the 1934 Bihar/Nepal earthquake ruptured along a 100-300 km long fault segment in eastern Nepal had ruptured (Pandey and Molnar, 1988; Bilham et al., 2001) with Ms about 8.2. In relation to this earthquake, the great earthquake of 1950 in Assam with M 8.6 had a rupture length of a few hundred km (Molnar, 1990; Bilham et al., 2001).

Several earthquake zones are found within the Central Himalaya region. One is located in a 550 km narrow belt along the High Himalaya front crossing from the west side of Nepal to the east side until it shifts 150km northward at 87°E (Pandey et al., 1999). Monsalve et al. (2006) also found a belt of microearthquakes along the front of the High Himalaya approximately 70 km wide at the point where the belt shifts northward (Figure 6). They state this area indicates a zone of stress accumulation during the interseismic period (Pandey et al., 1995; Monsalve et al.,

2006), which supports the high uplift rates of the High Himalaya (Lave and Avouac, 2001; Sheehan et al., 2008). Recordings from the HIMNT experiment also show earthquake alignment persisting below the region of highest relief (Figure 7). Due to the location on the hanging wall in the overlying thrust sheet, Monsalve et al., (2006) suggest the possible ramp and southern flat portions of the Main Himalaya thrust fault activate during larger earthquakes (Monsalve et al., 2006). Additional seismicity was found beneath the northern part of the network occuring at upper crustal depths that are related to the normal faults and grabens in South Tibet (Langin et al., 2003; Monsalve et al., 2006), while two other groups of earthquakes were found at lower crust and upper mantle depths. One group occurred between 30 and 70 km depth beneath South Nepal near the same location of the August 20th, 1988 6.5 magnitude earthquake (Pandey et al., 1999; Monsalve et al., 2006), and another occuring between 50 and 100 km depth beneath south Tibet and the High Himalaya (Monsalve et al., 2006). The first group of lower crust and upper mantle earthquakes are oriented northeast-southwest suggesting a subsurface structure (Monsalve et al., 2006). This zone is also centered at the same longitude where the microearthquake belt shifts northward, possibly marking the boundary of separate segments of the Himalayan Thrust fault.

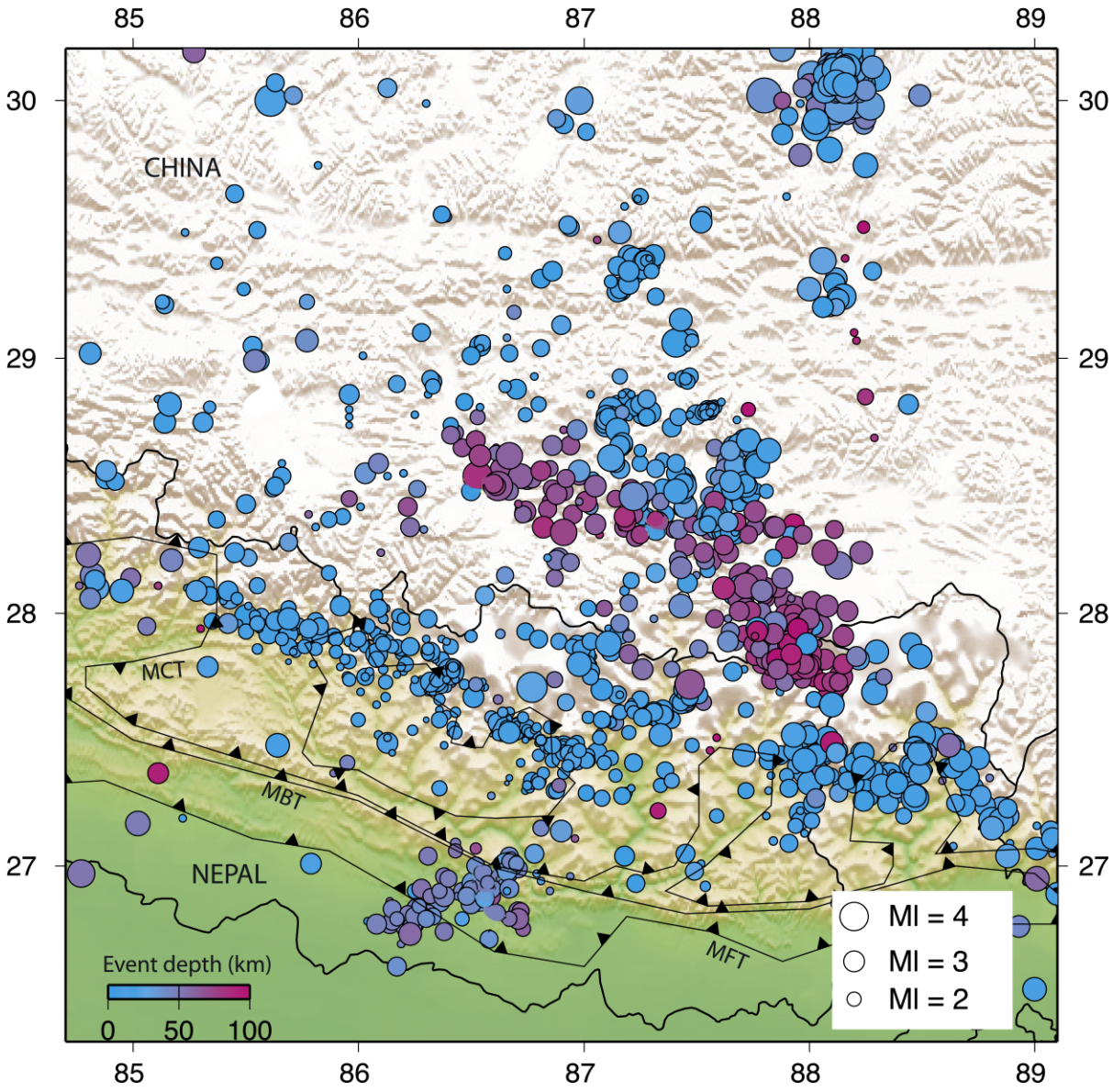

Figure 6: Map of the earthquake events from the Himalaya Nepal Tibet Seismic experiment displaying the belt of micro-earthquakes along the High Himalaya front in relation to the Main Central Thrust, Main Boundary Thrust and the Main Frontal Thrust (Monsalve et al., 2006).

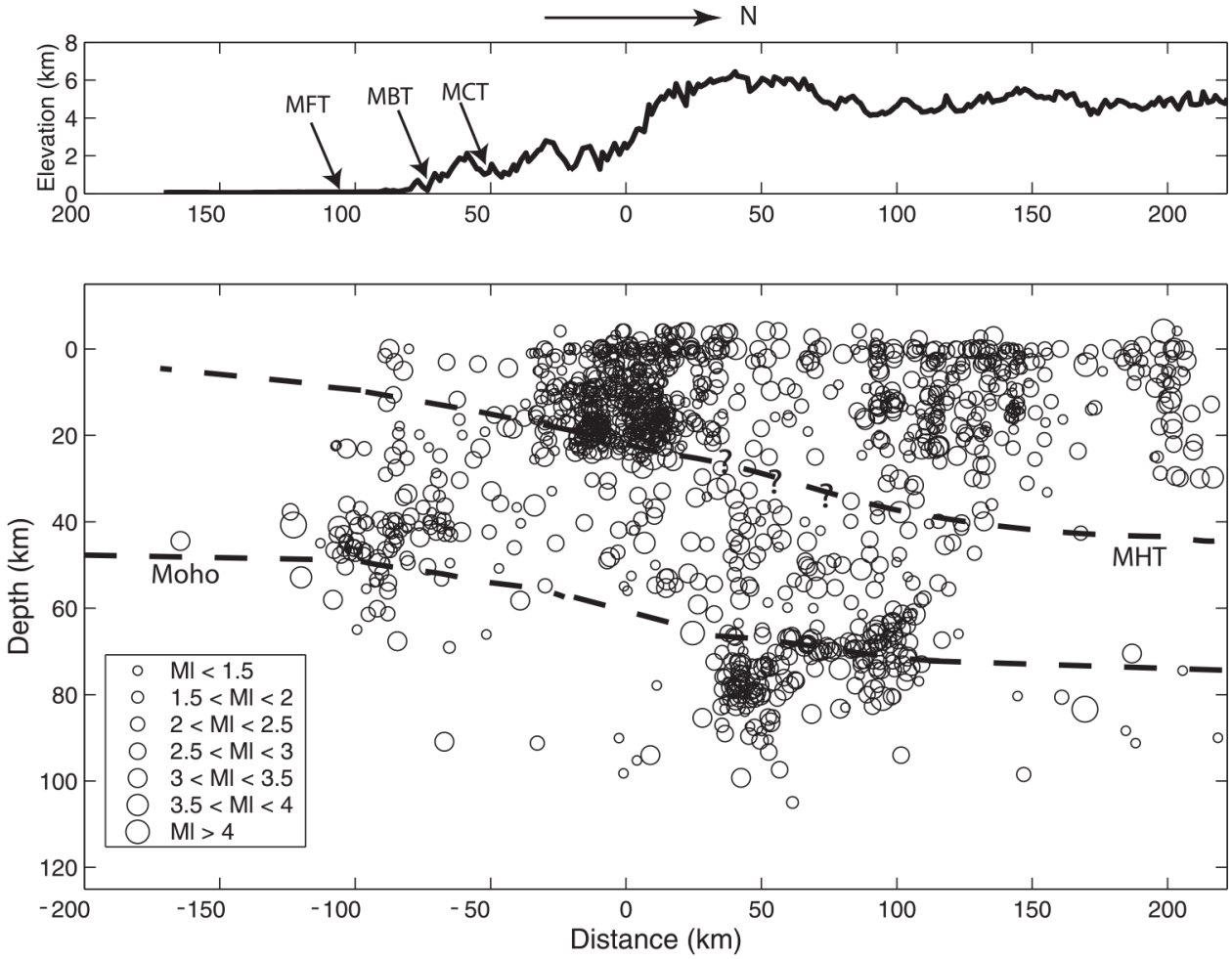

Figure 7: Earthquake to elevation and depth relationship from the Himalaya Nepal Tibet Seismic experiment with respect to 3 of the 5 shear zones, the Main Frontal Thrust (MFT), Main Boundary Thrust (MBT), and Main Central Thrust (MCT) (Monsalve et al., 2006).

Chapter 3: Data

3.1 Bhutan Deployment

The Bhutan deployment from January 2002 to March 2003 consisted of 5 broadband seismometers (Table 1) with a sampling rate of 40 samples per second. Three stations, DOCH, PARO, and TASH were Guralp 40T seismometers while the other two stations, CHUK and BUMT, were Strickheisen STS2s (Gee, 2005). During the deployment, ~2,100 events were recorded. The Antelope software package (Boulder Real Time Technologies) was used to process all waveforms and identify P- and S-wave arrivals at the termination of the array.

3.2 HIMNT Deployment

The overlapping HIMNT deployment from September 2001 to April 2003 consisted of 29 broadband seismometers (Table 1) with a sampling rate between 40 and 50 samples per second. All stations were Strickheisen STS2s (Monsalve et al., 2006). During this deployment over 1,500 events were recorded. I requested regional HIMNT data from Incorporated Research Institutions for Seismology Data Management Center (IRIS DMC) using FetchData. SEISAN earthquake analysis software was used to process this additional data and pick P- and S-wave arrivals.

3.3 Earthquake Data

Waveforms from both deployments comprised the earthquake dataset used to develop the velocity models for this experiment. I used 223 regional events from both the Bhutan and HIMNT deployments (Figure 8; de la Torre, 2005; Velasco et al., 2007). Regional events from the Bhutan deployment were chosen based on those that had the most P and S picks identified at the termination of the network. I requested these same events from the HIMNT experiment for additional coverage. Due to the extensive deformation in central Himalaya the earthquakes from both deployments did not have well defined S phases. Most of the waveforms showed a lot of noise, which affected identifying the precise location of each phase.

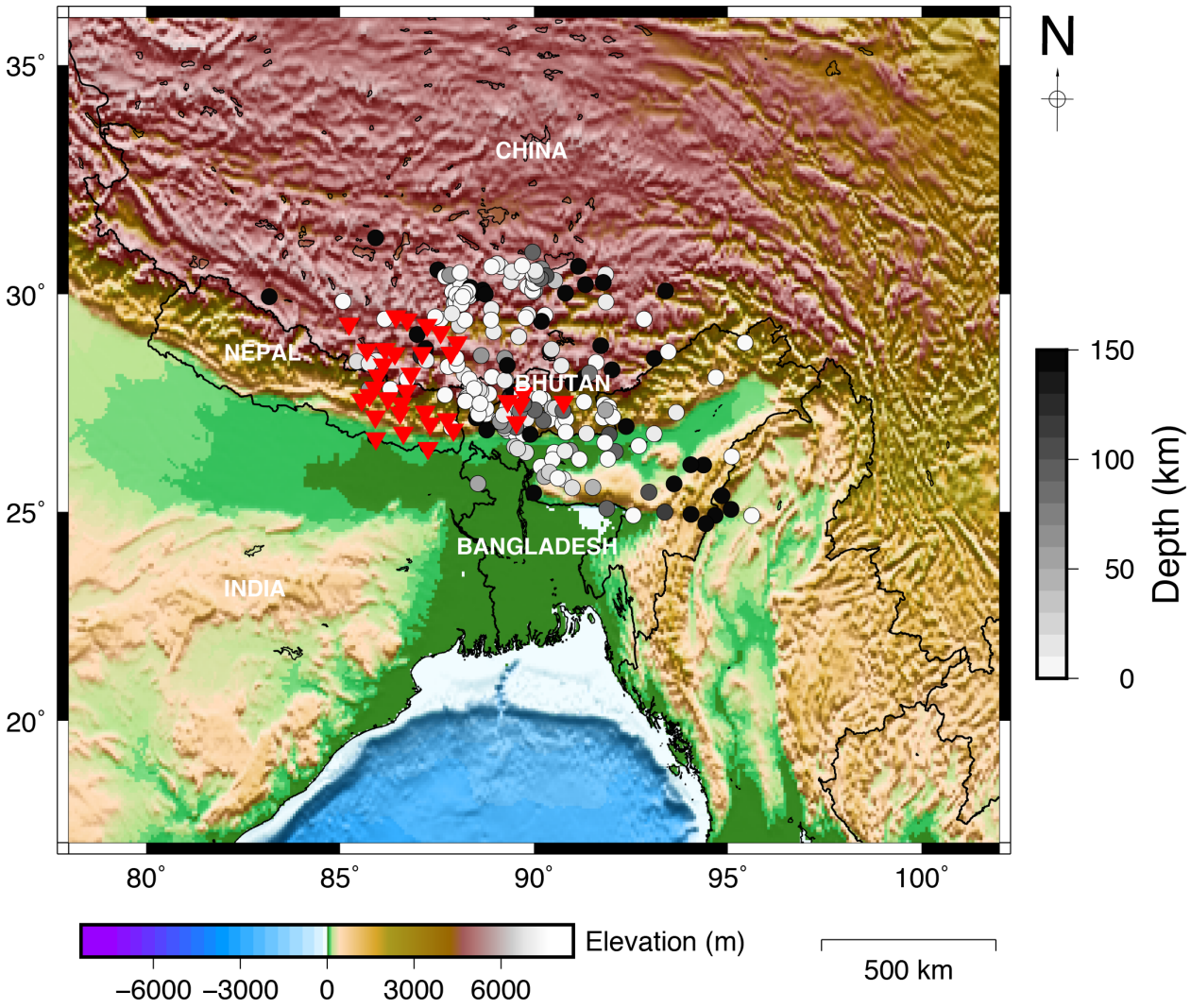

Figure 8: Map of 223 regional events (circles) used for the inversion recorded on both Bhutan and HIMNT arrays shown along with HIMNT seismic stations (de la Torre et al., 2005 and Bhutan seismic stations (Velasco et al., 2007) as red inverted triangles.

Table 1: Information on Seismic Stations of the Bhutan and HIMNT Networks

Station Code	Latitude N (deg.)	Longitude E (deg.)	Elevation (m)	Experiment
DOCH	27.49218	89.64347	3093	Bhutan
CHUK	27.08266	89.55026	2263	Bhutan
PARO	27.56732	89.32048	2566	Bhutan
BUMT	27.54765	90.76637	2772	Bhutan
TASH	27.7492	89.7309	1614	Bhutan
BIRA	26.484	87.267	12	HIMNT
BUNG	27.8771	85.8909	1191	HIMNT
DINX	28.6646	87.1157	4374	HIMNT
GAIG	26.838	86.6318	166	HIMNT
HILE	27.0482	87.3242	2088	HIMNT
ILAM	26.9102	87.9227	1181	HIMNT
JANA	26.7106	85.9242	77	HIMNT
JIRI	27.6342	86.2303	1866	HIMNT
LAZE	29.1403	87.5922	4011	HIMNT
MAZA	28.6713	87.8553	4367	HIMNT
MNBU	28.7558	86.161	4500	HIMNT
NAIL	28.6597	86.4126	4378	HIMNT
NAMC	27.8027	86.7146	3523	HIMNT
NLMU	28.1548	85.9777	3889	HIMNT
ONRN	29.302	87.244	4350	HIMNT
PHAP	27.515	86.5842	2488	HIMNT
PHID	27.1501	87.7645	1176	HIMNT
RBSH	28.1955	86.828	5100	HIMNT
RC14	29.4972	86.4373	4756	HIMNT
RUMJ	27.3038	86.5482	1319	HIMNT
SAGA	29.3292	85.2321	4524	HIMNT
SAJA	28.9093	88.0209	4351	HIMNT
SIND	27.2107	85.9088	465	HIMNT
SSAN	29.4238	86.729	4585	HIMNT
SUKT	27.7057	85.7611	745	HIMNT
THAK	27.5996	85.5566	1551	HIMNT
TUML	27.3208	87.195	360	HIMNT
XIXI	28.7409	85.6904	4660	HIMNT
YALA	28.4043	86.1133	4434	HIMNT

4. Method

4.1 Double-Difference Tomographic Inversion

I apply a double-difference tomographic inversion technique, TomoFDD (Zhang and Thurber, 2003), to further understand the velocity structure of central Himalaya. This technique jointly inverts for event relocations and a pre-defined seismic velocity structure (Zhang and Thurber, 2003). The program uses the double-difference relocation method of Waldhauser and Ellsworth (2000) that minimizes the error in determining hypocenter location and provides relocations of earthquakes by comparing event-station distance to the distance between two earthquake hypocenters recorded at a common station.

4.2 Waveform Cross Correlation and Travel Times

The distance between two earthquakes can be referred to as hypocentral separation or spatial offset (e.g., Waldhauser and Ellsworth, 2000). If two earthquakes have a small hypocentral separation compared to event-station distance, both earthquakes will follow a similar ray path to the common station. Thus, they will have a similar source and location, and they will produce similar waveforms at the common station. Waveform cross correlation can then be performed to obtain high-precision travel times for similar waveforms (Waldhauser and Ellsworth, 2000; Shearer, 1997). The time shift or differential travel-time data reduces error in travel-time estimation and thus improves event location (Waldhauser and Ellsworth, 2000; Zhang and Thurber, 2003).

An alternative to determining event relocations combines differential travel times through waveform cross correlation with original travel time picks (Shearer, 1997). This approach can eliminate having to use an assumed single reference location to relocate event pairs, with the limitation that relative location can only be solved using isolated sets of similar events (Shearer, 1997). Specifically, Shearer (1997) uses both picked times and differential times to invert for a new set of adjusted picks thereby minimizing the misfit to only those two values. The method I used, TomoFDD, is a combination of both types of relocation methods.

4.3 TomoFDD Algorithm

TomoFDD jointly inverts absolute and relative arrival times with a predefined velocity model to generate a synthetic velocity model for the region. TomoFDD works to minimize:

$$\frac{\partial t_k^{ij}}{\partial \mathbf{m}} \Delta \mathbf{m}^{ij} = dr_k^{ij} \tag{1}$$

where Δm^{ij} is change in relative hypocentral parameters between two events and the partial derivatives are components of the slowness vector of the ray connecting the source and receiver measured at the source (e.g., Aki and Richards, 1980). dr^{ij}_k is the difference between observed and theoretical travel times and can be extended to

$$dr_k^{ij} = (t_k^i - t_k^j)^{\text{obs}} - (t_k^i - t_k^j)^{\text{cal}}, \tag{2}$$

the double-difference (e.g., Waldhauser and Ellsworth, 2000).

Equation (1) assumes a constant slowness vector, but this is not a good approach when considering events that are not in proximity to one another. The change in hypocentral distance between two events, *i* and *j*, can instead be represented by the difference of a simplified equation (1)

$$\frac{\partial t_k^i}{\partial \mathbf{m}} \Delta \mathbf{m}^i - \frac{\partial t_k^i}{\partial \mathbf{m}} \Delta \mathbf{m}^j = dr_k^{ij} \tag{3}$$

(e.g., Waldhauser and Ellsworth, 2000). This equation is then combined with hypocentral pairs for all stations to form,

$$WGm = Wd \tag{4}$$

where *G* represents a *M* X *4N* matrix that contains the partial derivatives of Equation (3). Specifically, *M* is the number of double-difference observations and *N* is the number of events. *d* is the data vector that contains the double-differences. *m* is a vector of length of 4*N*, which defines the changes in hypocentral parameters being determined. *W* is the diagonal matrix used to weigh each equation (e.g., Waldhauser and Ellsworth, 2000).

Chapter 5: Checkerboard Tests

I performed checkerboard testing (e.g., Leveque et al., 1993) with TomoFDD and developed four velocity models. Checkerboard testing visually estimates the resolution of a derived model from a synthetic model of a repeating pattern of high and low velocities (Leveque et al., 1993). Using stations and event arrival times I computed travel times through this "checkerboard" and ran the joint tomographic inversion to determine if I could recover the original pattern of the 1-D starting model. Some areas of the checkerboards were not recovered which limited the overall interpretation of the region.

5.1 Checkerboard Model 1

For the first velocity model I used events and stations from the Bhutan deployment located between 85° and 95°E longitude, and 25° and 31°N latitude. A total of 121 regional events were used with a minimum of 5 P and S phase picks. Depths for these events ranged from 1 and 400 km. The maximum distance (MAXDIST) between event pairs and stations was 2,300 km. Earthquake clusters within this distance were identified as a maximum of 20 neighbors per event (MAXNGH) with a minimum number of 3 links per pair of events defining a neighbor (MINLNK). The hypocentral separation between these events was no greater than 100 km (MAXSEP). A minimum observation of 3 links (MINOBS) to a maximum observation of 200 links (MAXOBS) per event pair were saved as my differential travel-time catalog. The travel-time catalog created by the above parameters (Table 2) was then used to create synthetic differential travel-times to run with the inversion. Results of this synthetic velocity model is shown below (Figure 9).

5.2 Checkerboard Model 2

The second velocity model consisted of the same events and stations as velocity model 1. To keep my results consistent I kept the grid refined to 85° and 95°E longitude, and 25° and

Table 2: Cluster Parameters Used For Models 1-4

Model	**MAXDIST**	**MAXSEP**	**MAXNGH**	**MINLNK**	**MINOBS**	**MAXOBS**
Model 1	2300	100	20	3	3	200
Model 2	2300	200	50	3	3	200
Model 3	2300	100	20	3	3	200
Model 4	2300	100	20	3	3	200

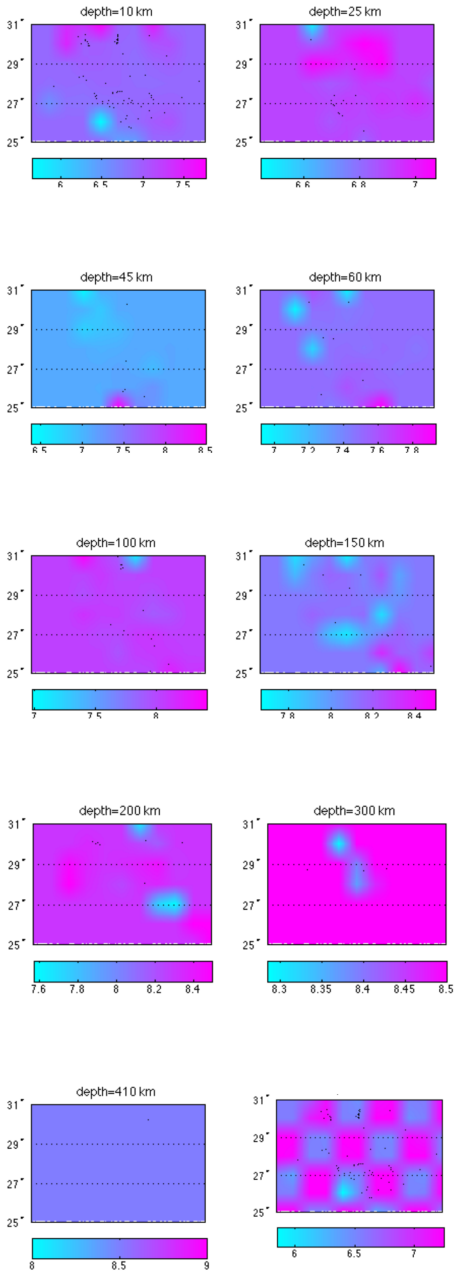

Figure 9: Checkerboard Model 1 displaying P-wave velocities with input velocity model on bottom right displayed with earthquakes (black dots). Scale bars are below each depth layer in km/s.

31°N latitude. To compare with my initial model, I redefined the parameters used to identify my earthquake clusters. The maximum distance between event pairs and stations remained 2,300 km. Earthquake clusters within this distance were now identified as a maximum of 50 neighbors per event, still with a minimum number of 3 links per pair defining a neighbor. I decreased the hypocentral separation between these events to 100 km and kept a minimum observation of 3 links to a maximum observation of 200 links per event pair to be saved as my differential travel-time catalog. Results of synthetic model 2 is shown below (Figure 10).

5.3 CHECKERBOARD MODEL 3

For the third velocity model, I used stations from both the Bhutan and Himalaya Nepal Tibet (HIMNT) deployments. The span of the HIMNT deployment is located ~5° west of the Bhutan deployment so I kept the same grid, 85° and 95°E longitude, and 25° and 31°N latitude. The regional events for this model totaled 223 events, still using a minimum of 5 P and S phase picks for each. Depths of these events ranged from 1 and 680 km. I kept the cluster parameters the same as the first velocity model: maximum distance between event pairs and stations, 2,300 km, earthquake clusters identified as a maximum of 20 neighbors per event with a minimum number of 3 links per pair of events defining a neighbor. Hypocentral separation between events did not exceed 100 km and minimum observation of 3 links to a maximum observation of 200 links per event pair was saved as my differential travel-time catalog. Results of this synthetic velocity model is shown below (Figure 11).

5.4 CHECKERBOARD MODEL 4

With the first three models showing similar output, I took a look at the travel-time error used to produce my differential travel-time catalog. Travel-time error for P-phases was 0.1 s and 0.5 s for S-phases. I ran model 4 exactly like model 3: 223 regional events with a minimum of 5 P and S picks at depths ranging from 1 to 680km, maximum distance between event pairs

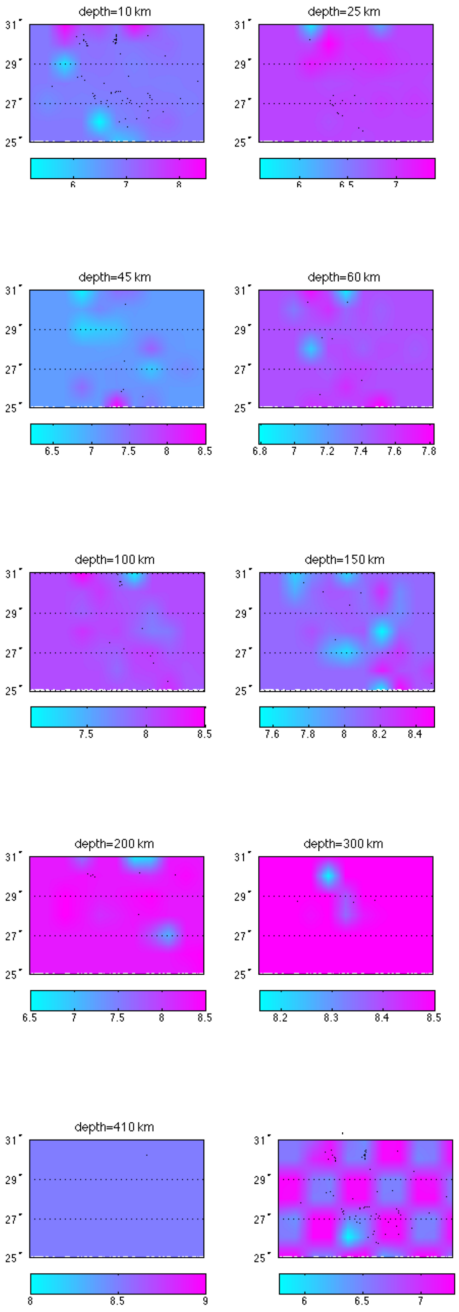

Figure 10: Checkerboard Model 2 displaying P-wave velocities with input velocity model on bottom right displayed with earthquakes (black dots). Scale bars are below each depth layer in km/s.

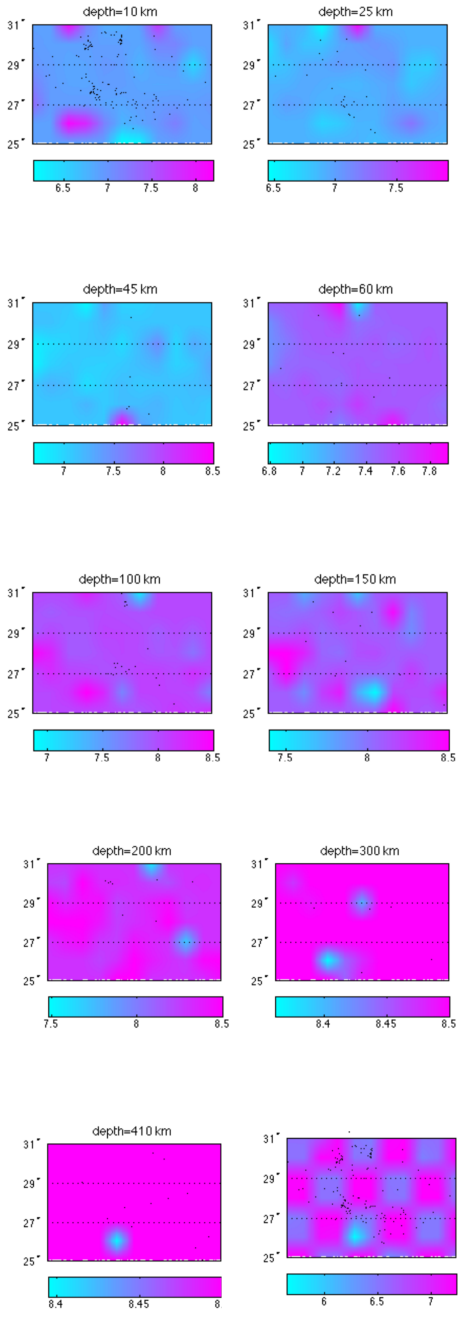

Figure 11: Checkerboard Model 3 displaying P-wave velocities with input velocity model on bottom right displayed with earthquakes (black dots). Scale bars are below each depth layer in km/s.

and stations at 2,300 km, earthquake clusters identified as a maximum of 20 neighbors per event with a minimum number of 3 links per pair of events defining a neighbor, hypocentral separation 100 km or less, and a minimum observation of 3 links to a maximum observation of 200 links per event pair. Results of this model can be seen below (Figure 12).

5.5 CHECKERBOARD MODEL 1-4 COMPARISON

The 1-D starting model used in TomoFDD was taken from Gee (2005) (Figure 2). This was the model jointly inverted with the synthetic models produced by the aforementioned parameters. All four models showed results at depths 10, 25, 45, 60, 100, 150, 200, 300, and 410 km. Models 1 and 2 showed similar recovery. Both displayed faint anomalies with a higher concentration at 100 and 150 km. The bottom most layer at 410 km did not show any recovery. This is most likely due to lack of ray path coverage in this layer. Models 3 and 4 showed better recovery than 1 and 2 in all layers, again with a higher concentration at 100 km and 150 km. The layer at 410 km displayed a minor anomaly in comparison to models 1 and 2.

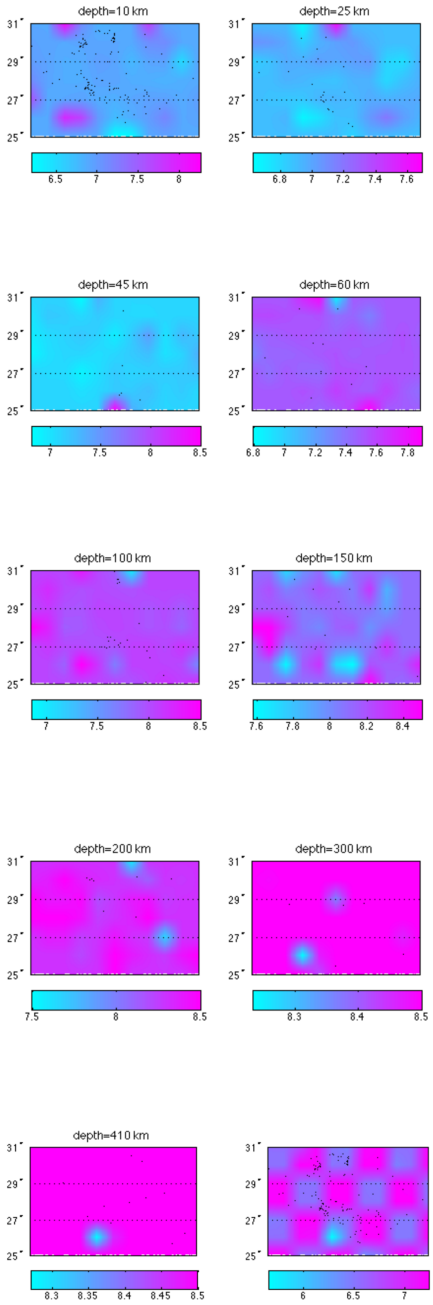

Figure 12: Checkerboard Model 4 displaying P-wave velocities with input velocity model on bottom right displayed with earthquakes (black dots). Scale bars are below each depth layer in km/s.

Chapter 6: Velocity Model

Based on my checkerboard results, I chose Checkerboard Model 4 to run my inversion and produced a 3-D velocity model (Figure 13) for central Himalaya. TomoFDD was set to recover specific depths between 10km and 410km. These values were 10km, 25km, 45km, 60km, 100km, 150km, 200km, 300km, and 410km. All depths were chosen based on the 1-D starting model (Figure 2) from Gee (2005). The majority of anomalies for the 3-D velocity model exist between 10 km and 150 km. This is most likely due to having more earthquake data for these lower velocity model depths.

Resolution for 25 km and 45 km is similar. Both display velocities consistent with upper crustal material (6.5 to 7.3 km/sec). This is not surprising since the crust in this region is very thick (up to 20 km) (Ni and Barazangi, 1984). At 45 km, upper mantle velocities (7.5 to 8.3 km/sec) were slightly resolved. This particular anomaly is oriented north-south and has a higher resolution at 60 km. These values are consistent with the idea that there could be channel flow beneath the Himalaya (Harris, 2007). For channel flow to exist in an area like the Himalayas, two things are required. One, the formation of a low-viscosity layer in the middle-lower crust and two, a lateral pressure gradient linked to contrasting elevations such as the plateau and foreland (Harris, 2007). Because of the intricacy of deformational areas within the Himalaya region, the Himalaya has a topographic load adequate for low-viscosity channel movement. Harris (2007) implies that while there is no hard evidence to support channel flow existing present day, the history of the Himalaya show models that should be considered when evaluating the time-frame channel flow has existed. The model developed by Hodges et al. (2001) (Figure 14), shows the presence of channel flow would create an extrusion-erosion mechanism where middle to lower crustal material gets extruded southward at Moho depth and then exhumed as ductile material in the area of highest relief followed by erosion.

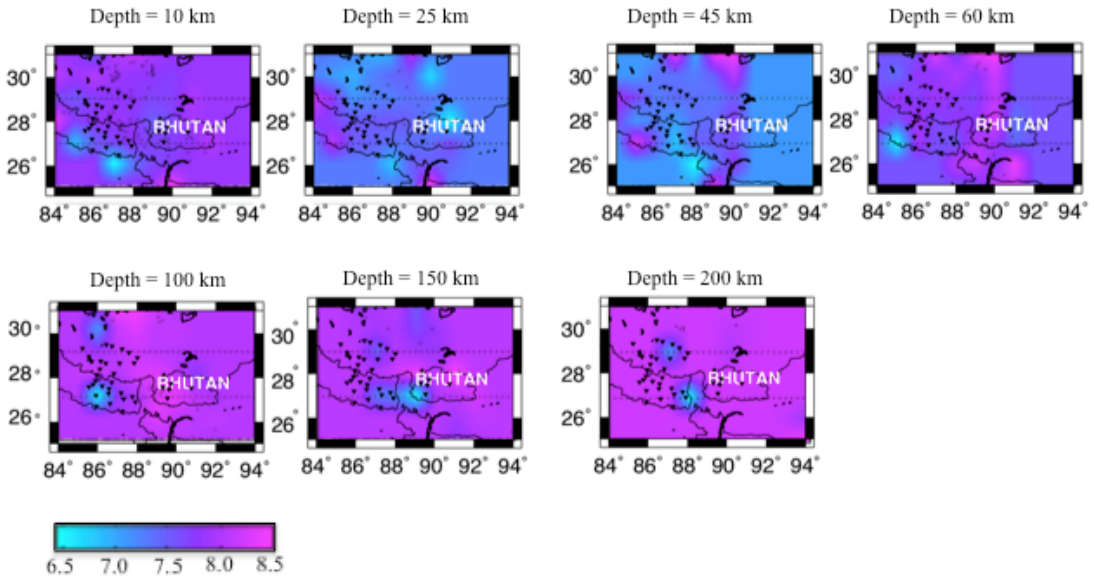

Figure 13: Results of TomoFDD inversion using Checkerboard Model 4 with earthquakes displayed as black dots and seismic stations displayed as black inverted triangles with the velocity scale on the bottom left in km/s.

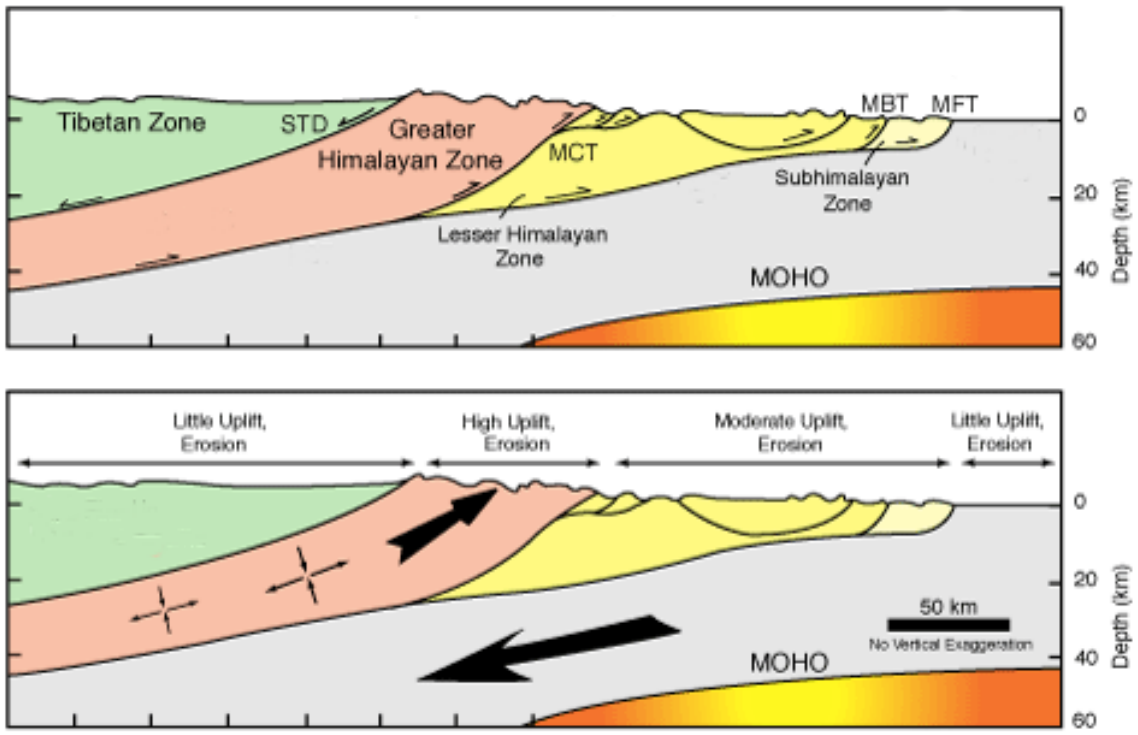

Figure 14: Cross-section displaying the process of channel flow beneath Himalaya. The different deformational zones are displayed as green, pink, yellow and grey regions. Black arrows show direction of plate movement toward the Moho followed by exhumation (modified from Hodges et al., 2001).

Chapter 7: Discussion

6.1 Recovered Velocity Model

The velocity model developed by TomoFDD did not show good recovery of a detailed velocity model for the central Himalaya. Even though I used the checkerboard model that incorporated the additional stations and events from the HIMNT deployment (Figures 11 and 12), the resolution still remained insufficient for extensive interpretation. I was able to identify an anomaly that could be consistent with possible channel flow in the middle-lower crust (Harris, 2007). The channel flow model developed by Hodges et al. (2001) (Figure 14) shows lower to middle crustal material being extruded slightly at 20km depth and then very extruded as depths approach the lower-crust upper-mantle transition zone. The ductile material is what I believe displays as the higher velocity values being resolved at 45km and 60km depth in my full inversion. As this mechanism also includes exhumation, both the HIMNT experiment and my experiment support this idea, as there is a large cluster of earthquakes persisting at the region of highest relief occurring at upper crustal depths (Figures 7 and 8). Also interesting to note is that the area where I resolved higher velocities is the same area Monsalve et al. (2006) found upper mantle earthquakes (Figure 6) in support of a hidden seismogenic structure. This is also the area Monsalve et al. (2006) identifies as a transverse feature marking the limit between different segments of the Main Himalayan Thrust. While the cross section of earthquakes does not show as much clustering at Moho depth (Figure 7) earthquakes are still oriented together and even more so at 60 and 80km depth, which could possibly support some type of mechanism driving earthquake activity.

6.2 Incorporating Teleseismic in TomoFDD

Using only regional data does not provide enough ray-path coverage to resolve central Himalaya in its entirety. Most of the waveforms showed a lot of noise due to the heterogeneity and complex crustal structure of the region (Figure 15). Because of this, phase picks are not as accurate as teleseismic phase picks would be. Even though I preemptively selected events with a

minimum of 5 P and S phase picks to improve the travel-time data, and kept my grid centered on both HIMNT and Bhutan earthquake clusters, this approach did not enable me to increase resolution enough to establish a well-defined earth model. Checkerboard Models 3 and 4 (Figures 11 and 12) displayed slightly better than Checkerboard Models 1 and 2 (Figures 9 and 10) implying that using more raypaths will increase the resolution for the resulting velocity model. TomoFDD does not have the capability to simultaneously invert regional waveforms and teleseismic waveforms with a starting velocity model. FMtomo is another joint inversion code that can handle travel times specific to both sets of events. I will attempt to use FMtomo (Appendix A) in the future to develop an earth model for central Himalaya and compare it to TomoFDD.

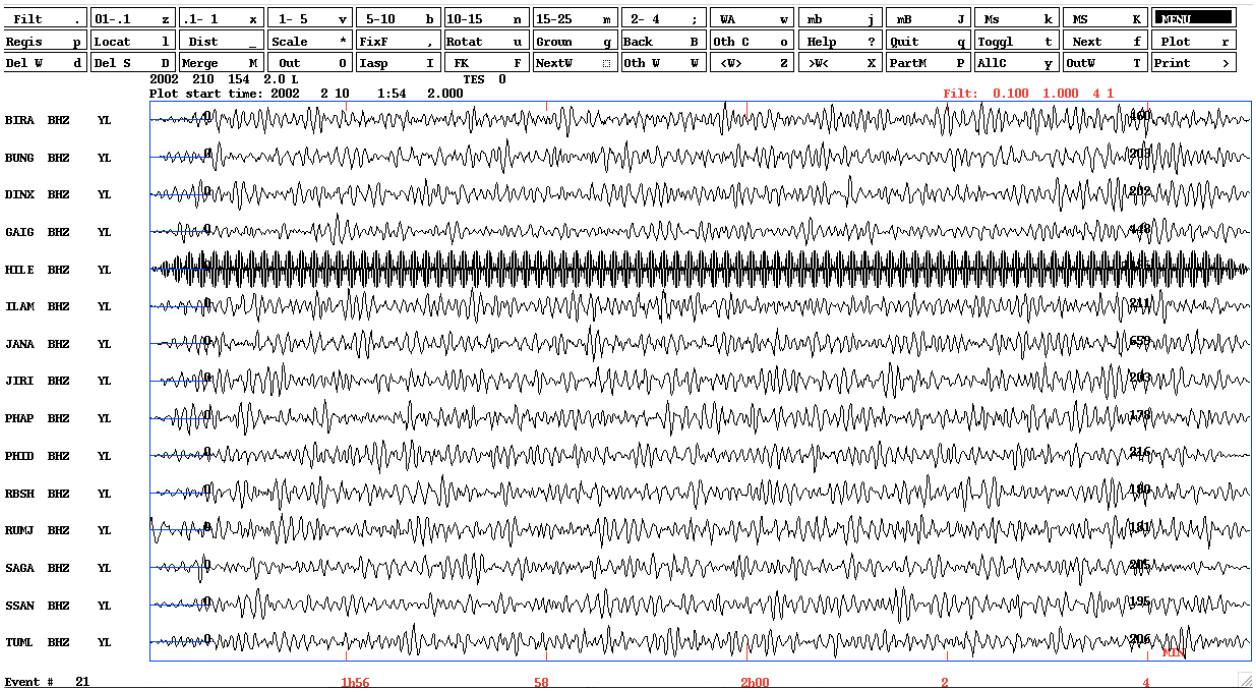

Figure 15: Display of noisy regional waveforms from the HIMNT experiment (de la Torre et al., 2005) recorded on the vertical component. These waveforms are shown with a 0.1 to 1.0 Hz filter.

Chapter 8: Conclusion

I utilize data from two temporary networks deployed in central Himalaya 2001-2003, the Bhutan deployment and the HIMNT deployment, to develop a 3-D velocity model of the central Himalaya using TomoFDD. TomoFDD jointly inverts event relocations with a defined starting velocity model to determine a 3-D structure. Four checkerboard tests were created using different parameters to pinpoint the best parameters for a full inversion but none showed enough resolution to provide a good earth model. The ray path coverage using only regional events was very limited. The resolution of the final velocity model showed possible channel flow but the resolution was still not enough to support any additional known or unknown crustal structures.

Incorporating teleseismic data, phases would improve regional raypath coverage increasing my ability to calculate travel time values to invert with a 1-D starting model. FMtomo would be a better option for future work based on its capability to run a simultaneous inversion for velocity using both regional and teleseismic events. Using this new technique I intend to confirm what we know about the crustal structure of the central Himalaya and extend the 1-D starting model (Gee, 2005) to a 3-D earth model to gain further insight on crustal accretion characteristics and earthquake-deformation relationships in the central Himalaya.

References

Aki, K., and P. G. Richards (1980). *Quantitative Seismology,* Vol. 2, W. H. Freeman, New York.

Ambraseys, N. and R. Bilham (2000), A note on the Kangra M_s = 7.8 earthquake of 4 April 1905, *Current Science, 79*, 45-50.

Bilham, R. (1995), Location and magnitude of the 1853 Nepal earthquake and its relation to the rupture zones of contiguous great Himalayan earthquakes, Current Science, 69, 101-128.

Bilham, R. (2001), Slow tilt reversal of the Lesser Himalaya between 1862 and 1992 at 78°E, and bounds to the southeast rupture of the 1905 Kangra earthquake, *Geophys. Jour. Intl.*, *144*, 713-728.

Bilham, R., V.K. Gaur, and P. Molnar (2001), Himalayan Seismic Hazard, *Science, 293*, 1442-1444.

Burg, J.P., A. Leyreloup, J. Girardeau, and G.M. Cheng (1987), Structure and metamorphism of a tectonically thickened continental crust: the Yalu Tsangpo suture zone (Tibet), *Philos. Trans. R. Soc. London, 321*, 67-86.

Carosi, R., C. Montomoli, and D. Visonà (2007), A structural transect in the Lower Dolpo: Insights on the tectonic evolution of Western Nepal*, J. Asian Earth Sci., 29*, 407–423.

Carosi, R., C. Montomoli, D. Rubatto, and D. Visonà (2010), Late Oligocene high-temperature shear zones in the core of the Higher Himalayan Crystallines (Lower Dolpo, western Nepal), *Tectonics, 29*, TC4029.

Chopp, D. (1993), Computing Minimal Surfaces via Level Set Curvature Flow, *Journal of Computational Physics, 106*, 77-91.

Copley, A., J. P. Avouac, and J. Y. Royer (2010), India-Asia collision and the Cenozoic slowdown of the Indian plate: Implications for the forces driving plate motions, *J. Geophys. Res., 115*, B03410.

Corrie, S. L., and M. J. Kohn (2011), Metamorphic history of the central Himalaya, Annapurna region, Nepal, and implications for tectonic models, *Geol. Soc. Am. Bull., 123*, 1863–1879.

de la Torre, T., and A. Sheehan (2005), Broadband seismic noise analysis of the Himalayan Nepal Tibet seismic experiment, *Bull. Seismol. Soc. Am., 95*, 1202-1208.

Dewey, J.F. and J.M. Bird (1970), Mountain belts and the new global tectonics, *J. Geophys. Res., 75*, 2625-2647.

Dewey, J.F. and K.C.A Burke (1973), Tibetan, Variscan, and Precambrian Basement Reactivation: Products of Continental Collision, *J. Geol., 81*, 683-692.

Drukpa, D., A.A. Velasco, and D.I. Doser (2006), Seismicity in the Kingdom of Bhutan (1937–2003), evidence for crustal transcurrent deformation, *J. Geophys. Res.-Solid Earth, 111,* B06301.

Dziewonski, A. M., T.A. Chou and J. H. Woodhouse (1981), Determination of earthquake source parameters from waveform data for studies of global and regional seismicity, *J. Geophys. Res.*, *86*, 2825-2852.

Ekström, G., M. Nettles, and A. M. Dziewonski (2012), The global CMT project 2004-2010: Centroid-moment tensors for 13,017 earthquakes, *Phys. Earth Planet. Inter.*, *200-201*, 1-9.

Gee, V. (2005). A Study Of The Crustal Structure Of The Himalaya In The Kingdom Of Bhutan, *Master's Thesis*, The University of Texas at El Paso.

Goscombe, B., D. Gray, and M. Hand (2006), Crustal architecture of the Himalayan metamorphic front in eastern Nepal, *Gondwana Res., 10(3)*, 232–255.

Harris, N. (2007), Channel flow and the Himalayan–Tibetan orogen: a critical review. *Journal of the Geological Society of London*, *164*, 511–523.

Hodges, K. V. (2000), Tectonics of the Himalaya and southern Tibet from two perspectives, *Geol. Soc. Am. Bull., 112*, 324–350.

Hodges, K.V., Hurtado, J.M., Whipple, K.X. (2001), Southward extrusion of Tibetan crust and its effect on Himalayan tectonics. *Tectonics*, *20*, 799–809.

Imayama, T., T. Takeshita, K. Yi, D. Cho, K Kitajima, Y. Tsutsumi, M. Kayama, H. Nishido, T. Okumura, K. Yagi, T. Itaya, Y. Sano (2012), Two-stage partial melting and contrasting cooling history within the Higher Himalayan Crystalline Sequence in the far-eastern Nepal Himalaya, *Lithos, 134*, 1–22.

Khanal, S., Robinson, D.M., and Kohn, M.J. (2015), Evidence for a far traveled thrust sheet in the Greater Himalayan thrust system, and an alternative model to building the Himalaya, *Tectonics, 34*, 31-52.

Kohn, M. J., M. Wieland, C. D. Parkinson, and B. N. Upreti (2004), Miocene faulting at plate tectonic velocity in the Himalaya of central Nepal, *Earth Planet. Sci. Lett., 228*, 299–310.

Lave, J., and J. P. Avouac (2001), Fluvial incision and tectonic uplift across the Himalayas of central Nepal, *Journal of Geophysical Research-Solid Earth, 106 (B11)*, 26561-26591.

LeFort, P . (1975), Himalayas: The collided range. Present knowledge of the continental arc, *Amer. J. Sci., 275A*, 1-44.

Leveque, J., L. Rivera, and G. Wittlinger (1993), On the use of the checker- board test to assess the resolution of tomographic inversions, *Geophys. J. Int., 115*, 313–318.

Mattauer M. (1986), Intracontinental subduction, crustal stacking wedge and crust- mantle decollement, *Geol. Soc. Lond. Spec. Publ., 19*, 37–50.

Molnar, P. (1990), A review of the seismicity and the rates of active underthrusting and deformation at the Himalaya, *Journal of Himalayan Geology, 1*, 131-154.

Molnar, P., and P. Tapponnier (1975), Cenozoic tectonics of Asia: Effects of a continental collision, *Science, 189*, 419–426.

Montomoli, C., S. Iaccarino, R. Carosi, A. Langone, and D. Visonà (2013), Tectonometamorphic discontinuities within the Greater Himalayan Sequence in Western Nepal (Central Himalaya): Insights on the exhumation of crystalline rocks, *Tectonophysics, 608*, 1349-1370.

Monsalve, G., A.F. Sheehan, V. Schulte-Pelkum, S. Rajaure, M.R. Pandey, and F. Wu (2006), Seismicity and 1-D velocity structure of the Himalayan collision zone: earthquakes in the crust and upper mantle. *J. Geophys. Res., 111*, B10301.

Ni, J., and M. Barazangi (1984), Seismotectonics of the Himalayan Collision Zone: Geometry of the underthrusting Indian plate beneath the Himalaya, *J. Geophys. Res., 89*, 1147–1163.

Osher, S., and J. Sethian (1988), Fronts Propagating with Curvature Dependent Speed: Algorithms Based on Hamilton-Jacobi Formulations, *Journal of Computational Physics, 79*, 12-49.

Pandey, M.R., and P. Molnar (1988), The distribution of intensity of the Bihar-Nepal earthquake of 15 January 1934 and bounds on the extent of the rupture zone, *Journal of Nepal Geological Society, 5*, 22-44.

Pandey, M., R. Tandukar, J. Avouac, J. Lave, and J. Massot (1995), Inter- seismic strain accumulation on the Himalayan crustal ramp (Nepal), *Geophys. Res. Lett., 22*, 751–754.

Pandey, M., R. Tandukar, J. Avouac, J. Vergne, and T. Heritier (1999), Seismotectonics of the Nepal Himalaya from a local seismic network, *J. Asian Earth Sci., 17*, 703–712.

Ratschbacher, L., W. Frisch, and L. Guanghua (1994), Distributed deformation in southern and western Tibet during and after the India-Asia collision, *J. Geophys. Res., 99*, 19,917–19,945.

Rawlinson, N., A. M. Reading, and B. L. N. Kennett (2006), Lithospheric structure of Tasmania from a novel form of teleseismic tomography, *J. Geophys. Res., 111*, B02301.

Rawlinson, N., and M. Sambridge (2003), Seismic traveltime tomography of the crust and lithosphere, *Advances in Geophysics, 46*, 81–198.

Rouy, E., and A. Tourin (1992), A Viscosity Solutions Approach to Shape-From-Shading, *SIAM Journal of Numerical Analysis, 29*, 867-884.

Seeber, L. and J.G. Armbruster (1981). Great detachment earthquakes along the Himalayan arc and long-term forecasting. In *Earthquake Prediction: An International Review*, Maurice Ewing Series, Vol. 4, D. W. Simpson, P. G. Richards, Washington, DC, 1981, pp. 259–277.

Seeber, L., J. Armbruster, and R. Quittmeyer (1981), Seismicity and continental collision in the Himalayan arc, in Zagros, Hindu-Kush, Himalaya, *Geodynamic Evolution, Geodyn. Ser., 3*, 215-242.

Sethian, J.A. (1982), An Analysis of Flame Propagation, *Ph.D.Dissertation (Univ. of California, Berkeley)*.

Sethian, J. A. (1985), Curvature and the evolution of fronts, *Comm. Math. Phys. 101*, 487-499.

Sethian, J. A. (1990), Numerical algorithms for propagating interfaces: Hamilton-Jacobi equations and conservation laws, *J. Differential Geom., 31*, 131-161.

Sethian, J.A. (1996), A fast marching level set method for monotonically advancing fronts: *Proceedings of the National Academy of Sciences, 93*, 1591–1595.

Sethian, J.A., and A.M. Popovici (1999), 3-D traveltime computation using the fast marching method, *Geophysics, 64***,** 516–523.

Shearer, P. (1997), Improving local earthquake locations using the L1 norm and waveform cross correlation: application to the Whittier Narrows, California, aftershock sequence, *J. Geophys. Res., 102***,** 8269–8283.

Sheehan, A.F., T. de la Torre, G. Monsalve, V. Schulte-Pelkum, R. Bilham, F. Blume, R. Bendick, F. Wu, M.R. Pandey, S. Sapkota, S. Rajaure (2008), Earthquakes and crustal structure of the Himalaya from the Himalayan Nepal Tibet Seismic Experiment (HIMNT), *J. Nepal Geol. Soc., 38*, 1-8.

Velasco, A.A., V. L. Gee, C. Rowe, D. Grujic, L. S. Hollister, D. Hernandez, K. C. Miller, T. Tobgay, M. Fort and S. Harder (2007), Using small, temporary seismic networks for investigating tectonic deformation: Brittle deformation and evidence for strike slip faulting in Bhutan, *Seismol. Res. Lett., 23***,** 435–438.

Waldhauser, F., and W. L. Ellsworth (2000), A double-difference earthquake location algorithm: Method and application to the northern Hayward fault, California, *Bull. Seism. Soc. Am., 90***,** 1353–1368.

Zhang, H., and C. H. Thurber (2003), Double-difference tomography: the method and its application to the Hayward fault, California, *Bull. Seism. Soc. Am., 93***,** 1875–1889.

Appendix A

I will apply a Fast Marching Method (FMM) to resolve a 3-D velocity model for central Himalaya. This fast marching method implements a fast scheme for solving the Eikonal equation (Sethian, 1996). More specifically, this method solves the equation by constructing traveltimes in an upwind fashion (Sethian and Popovici, 1999).

1.1 Entropy finite difference solution

FMM requires an understanding of a boundary separating one region from another, in particular, a surface in three dimensions or a curve in two dimensions. If this curve were to move with a known speed function of F, then the boundary interface evolves (Sethian, 1996). As the interface propagates, corners and discontinuities can develop (Figure a1-A.) thereby needing a weak solution to smooth out the interface (Sethian, 1982; Sethian, 1985; Sethian, 1990; Sethian, 1996). In order to implement the correct weak solution an entropy condition must be enforced by examining the limit of smooth solutions (Sethian, 1996). This can be expressed by

$$F = 1 - \varepsilon\kappa \quad (1)$$

(Figure a1-B.) where κ introduces curvature and ε is some constant (Sethian 1985). As ε goes to zero, the weak solution is produced (Figure a1-C.)

1.2 The upwind scheme

If a wave progresses left to right, a difference scheme should be used that reaches upwind to the left for information to create a solution downwind to the right (Sethian and Popovici, 1999). The upwind scheme used in fast marching can be represented by the Eikonal equation,

$$|\nabla u\,(x, y, z)| = s\,(x, y, z)$$

with $u\,(x, y, z)$ representing the traveltime field, and $s\,(x, y, z)$ representing a slowness function in the 3-D model (Sethian and Popovici, 1999). The Eikonal equation represented above is simply a measure of the arrival time gradient as a wave front propagates through a grid that is inversely proportional to the speed of the wave front. If $u\,(x, y)$ represents the time a curve, or wave front, passes the point x, y, then $u\,(x, y)$ satisfies,

$$|\nabla u|\, F = 1$$

(Sethian, 1996; Sethian and Popovici, 1999). When equation 2 is extended to the gradient, to multidimensions, the scheme (Osher and Sethian, 1988; Sethian and Popovici, 1999) can be shown as,

$$\begin{aligned} |\nabla u| \approx\ & (max(D_{ijk}^{-x}u, 0)^2 + min(D_{ijk}^{+x}u, 0)^2 \\ & + max(D_{ijk}^{-y}u, 0)^2 + min(D_{ijk}^{+y}u, 0)^2 \\ & + max(D_{ijk}^{-z}u, 0)^2 + min(D_{ijk}^{+z}u, 0)^2 \end{aligned}$$

where D^{-y}, D^{+y}, D^{-z}, D^{+z} are forward and backward operators similar to those defined in the x-direction.

A more convenient upwind scheme (Rouy and Tourin, 1992) for fast marching can be shown as,

$$\begin{bmatrix} max(D_{ijk}^{-x}u, -\left(D_{ijk}^{+x}u, 0\right)^2 + \\ max(D_{ijk}^{-y}u, -\left(D_{ijk}^{+y}u, 0\right)^2 + \\ max(D_{ijk}^{-z}u, -\left(D_{ijk}^{+z}u, 0\right)^2 \end{bmatrix}^{1/2} = S_{ijk}$$

where D^- and D^+ represent the same forward and backward operators but S_{ijk} represents the slowness at grid point (i,j,k) (Sethian and Popovici, 1999).

1.3 THE UPWIND SCHEME IN FAST MARCHING

Equation 5 shows that information propagates in one direction from smaller traveltime values represented by $u\ (x, y, z)$, to larger traveltime values (Sethian and Popovici, 1999). The algorithm is fast because the building zone is confined to a narrow band around the wave front using narrow-band technology (Chopp, 1993; Sethian and Popovici, 1999). The wave front is swept ahead in an upwind fashion by considering a set of points in the narrow band around the wave front and the band is marched forward freezing the values of existing points while new ones are being brought into the narrow band (Figure 2).

This approach essentially keeps track of first arrival wave fronts as they propagate using a causal narrow-band evolution scheme with an upwind scheme that has an entropy-satisfying

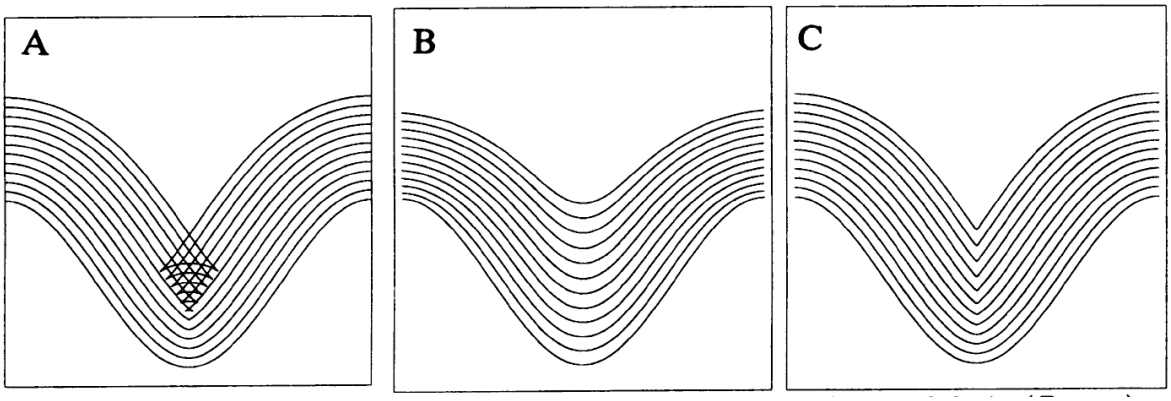

Figure a1: A) Display of a corner developed in a propagating wave front, B) Implementation of $F=1 - \varepsilon\kappa$ to account for curvature and obtain a weak solution, C) Display of the weak solution.

finite difference solution for the Eikonal equation (Rawlinson et al., 2006). In essence, this technique is very much like Huygens principle. As a wave front propagates, or rather, the narrow band marches; it touches the next grid point and recomputes all nearby values (Sethian, 1996; Sethian and Popovici, 1999).

1.4 COMPUTING THE ALGORITHM

To begin the fast marching algorithm, I established the points that met initial conditions as accepted. I then defined the points located one grid point away from the accepted point as "close", the narrow band of trials. All other grid points are classified as "far away" (Sethian, 1996; Sethian and Popovici, 1999). After these initial conditions are set, the fast marching algorithm completes a loop by the following process:

1). Begin loop: Let trial be the point in narrow band with the smallest value for u.

2). Add the point to accepted values and remove it from the narrow band.

3.) Tag values that were not accepted in the narrow band and values that were "far away" as neighbors. If the values were "far away", move them to the narrow band.

4.) Re-compute the values of u for all narrow band neighbors using equation (5).

5.) Return to the top of the loop.

1.5 FAST MARCHING METHOD INVERSION

There are two ways FMM uses traveltimes to develop a velocity model, either by inverting for source parameters or inverting for interface depth and velocity node parameters (Rawlinson et al., 2006). I use the option that inverts for interface depth and velocity node parameters using both regional and teleseismic datasets. With this option a pre-defined velocity model can be established as the *a priori* model for the simultaneous inversion between both datasets. It also allows for interfaces and layers to be defined that are dependent on a path signature associated with each traveltime. FMM works to minimize the difference between observed and theoretical traveltimes while also adding a damping factor for outputs that may be

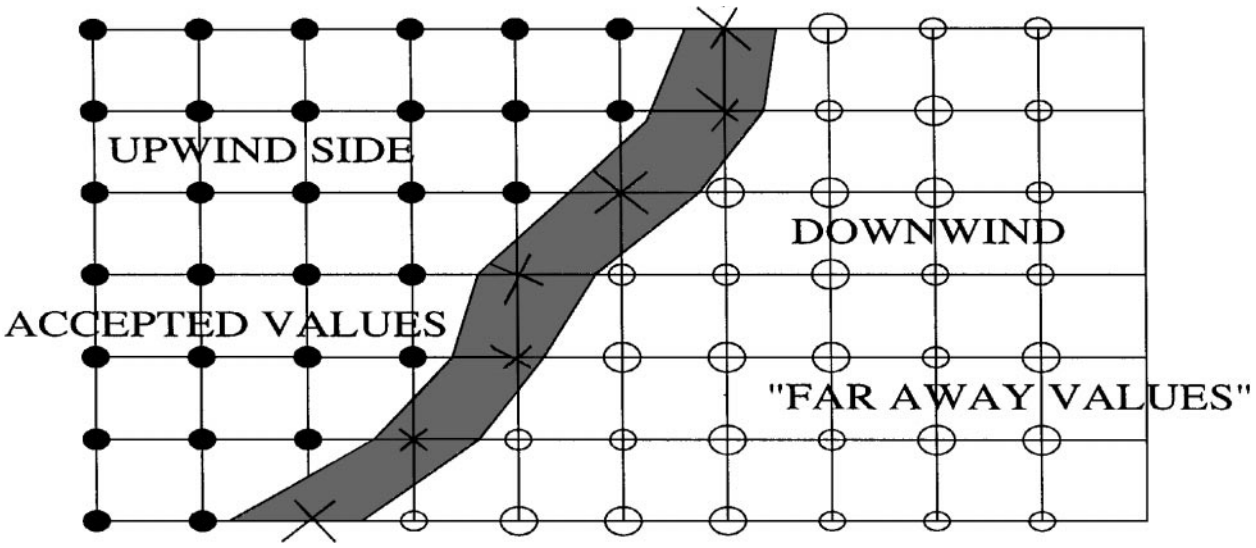

Figure a2: Schematic diagram of accepted values in an upwind construction with the grey block representing the narrow band of trial values at the wave front (modified from Sethian and Popovici, 1999).

far from the starting model (Rawlinson et al., 2006). FMM also accepts uncertainty values specific to regional traveltimes and traveltime residuals specific to teleseismic traveltimes. The FMM iteration is performed consecutively with a subspace inversion scheme. With this scheme, a minimization is performed simultaneously in several directions that essentially map a subspace in the model space (Rawlinson and Sambridge, 2003; Rawlinson et al., 2006). The combination of both FMM iterations and the subspace inversion scheme is what accounts for the non-linear relationship between traveltime and wave speed (Rawlinson et al., 2006).

Curriculum Vita

Chanel Ashlie Perez was born in Bronx, New York and raised in Patterson, New York. The third of four children of David and Sharon Perez, she was the first of her siblings to receive her Bachelor's degree from Central Connecticut State University May 2013. She majored in Geology and presented her first work at the 48th GSA Northeastern Section Annual Meeting. During this time Chanel also had the opportunity of pursuing an international volcanology field camp in Petropavlosky-Kamchatsky, Russia to explore her original interest in Geophysics and Seismology. In 2013, she was accepted into the Geophysics Master's program at The University of Texas at El Paso where she was offered a Teaching Assistantship and had the opportunity to instruct Physical and Historical Geology laboratories. In this same year Chanel was voted Treasurer of the Society of Exploration Geophysics and then Vice President the following year. After the completion of her first year in the Master's program Chanel was fortunate enough to receive a summer internship at Los Alamos National Laboratory where she was able to incorporate her Master's research into her daily job routine. Chanel was awarded a fellowship during her second year at The University of Texas at El Paso as a GK-12 fellow where she taught at a local early college high school and exposed students to her own research. She helped teach Physics, Engineering and college-credit physics courses. Chanel was able to present a portion of her Master's work at the 47th Annual American Geophysical Union meeting where got news she was going to start her first Geophysical position at Leidos Corporation as a government contractor. Being the only one out of her family that did not join the military Chanel was bound to find something in Geophysics that benefited people other than herself just as the military would. She was able to reach this goal when she completed her Master's degree early and moved across the United States to begin her career at Leidos Corporation, a company that actively participates in efforts to develop national security solutions.

Contact Information:

1031 Cascade Circle, Apt 107

Rockledge, FL 32955

Or

caperez14@miners.utep.edu